

From mixed valence to the Kondo lattice regime

Pramod Kumar and N. S. Vidhyadhiraja

Theoretical Sciences Unit,
Jawaharlal Nehru Centre for Advanced Scientific Research,
Bengaluru 560064, India.

Abstract. Many heavy fermion materials are known to crossover from the Kondo lattice regime to the mixed-valent regime or vice-versa as a function of pressure or doping. We study this crossover theoretically by employing the periodic Anderson model within the framework of the dynamical mean field theory. Changes occurring in the dynamics and transport across this crossover are highlighted. As the valence is decreased (increased) relative to the Kondo lattice regime, the Kondo resonance broadens significantly, while the lower (upper) Hubbard band moves closer to the Fermi level. The resistivity develops a two peak structure in the mixed valent regime: a low temperature coherence peak and a high temperature ‘Hubbard band’ peak. These two peaks merge yielding a broad shallow maximum upon decreasing the valence further. The optical conductivity, likewise exhibits an unusual absorption feature (shoulder) in the deep mid-infrared region, which grows in intensity with decreasing valence. The involvement of the Hubbard bands in dc transport, and of the effective f -level in the optical conductivity are shown to be responsible for the anomalous transport properties. A two-band hybridization-gap model, which neglects incoherent effects due to many-body scattering, commonly employed to understand the optical response in these materials is shown to be inadequate, especially in the mixed-valent regime. Comparison of theory with experiment carried out for (a) dc resistivities of CeRhIn₅, Ce₂Ni₃Si₅, CeFeGe₃ and YbIr₂Si₂; (b) pressure dependent resistivity of YbInAu₂ and CeCu₆; and (c) optical conductivity measurements in YbIr₂Si₂ yields excellent agreement.

PACS numbers: 71.27.+a Strongly correlated electron systems; heavy fermions - 75.20.Hr Local moment in compounds and alloys; Kondo effect, valence fluctuations, heavy fermions

Submitted to: *J. Phys. Condens. Matter*

1. Introduction

Rare earth lanthanides and actinides [1, 2] exhibit a wide range of behaviour such as heavy fermions (HFs), mixed valence (MV), proximity of superconductivity and magnetism, quantum critical points etc. Such behaviour arises through an interplay of a variety of factors such as hybridization between conduction bands and deep f -levels, orbital degeneracy, crystal field effects, long range spin interactions and most importantly local Coulomb repulsion [3–7].

In this work, we present a detailed and systematic theoretical investigation of a regime that borders on heavy fermions at one end and on the mixed valence regime at the other. Experimentally, such a crossover from HFs to MV or vice-versa has been observed to happen through pressure or doping [8–11]. The effects of such a crossover have been investigated for several materials [12–21]. For example, the first known heavy fermion superconductor CeCu_2Si_2 [9], when doped with Yttrium (a non-magnetic homologue of Ce) shows increasing mixed valent character. The resistivity exhibits a two peak structure in the temperature range 2K to 300K. Varying doping concentration results in gradual coalescing of the two peak structure into a single broad peak. For the heavy fermion compound YbCu_4Ag [10], the ambient pressure resistivity as a function of temperature shows a broad peak which is characteristic of mixed valent compounds. By applying pressure, the broad peak sharpens and the peak position also shifts to lower values of T , thus indicating a crossover to the Kondo lattice regime. The T^2 coefficient of the low temperature Fermi-liquid resistivity also increases sharply with pressure, implying a decrease in the coherence scale. CeBe_{13} [11] also shows a pressure-induced crossover from Kondo lattice regime to mixed-valent regime, as seen in the changes in the coherence peak in the resistivity. The trend in this material is opposite to that seen in the previous example, YbCu_4Ag . [10]

Most previous theoretical attempts to describe the effects of pressure on heavy fermion materials have employed the single-impurity Anderson model [22–24]. An illustrative and important work in this context is that of Chandran et al [22]. They use a phenomenological model comprising a competition between elastic energy cost and valence fluctuations induced magnetic energy gain. The magnetic energy for an Anderson lattice model was computed by using the free energy of an impurity Anderson model and ignoring lattice coherence effects. The free energy itself was arrived at through a slave-boson mean field approximation [25] which is a static approximation and is thus unable to treat dynamical effects of valence fluctuations. Phenomenological expressions were used to model volume dependence of the parameters, and the pressure was obtained by using $P(T, V) = -\partial F/\partial V$. The authors were able to describe continuous and discontinuous valence transitions in a single framework. However, since the impurity Anderson model was used, lattice coherence effects were ignored. Transport quantities were not calculated. Recent years have seen the use of lattice models to describe the concentrated Kondo systems. The minimalist model that accounts for a large part of heavy fermion and mixed-valent behaviour is the periodic Anderson

model (PAM) which represents a lattice of localized f -orbitals with a Hubbard repulsion U hybridizing locally with a wide non-interacting conduction band. The PAM has of course been explored extensively using a wide range of methods and techniques such as dynamical mean field theory (DMFT) [26, 27], extended DMFT [28], cluster expansions [29], finite size simulations [30] etc. Within the framework of dynamical mean field theory (DMFT) [26, 27], the self-energy becomes purely local or momentum independent, which simplifies the problem significantly, while retaining the competition between itinerancy and localization in a non-trivial way. The momentum independence of the self-energy implies that we can view lattice problems as locally self-consistent impurity problems, hence the solution of PAM, for instance reduces to that of a single-impurity Anderson model with a self-consistent hybridization. The various impurity solvers that have been adapted to solve the effective impurity problem are numerical renormalization group [31], quantum Monte Carlo [32], exact diagonalization [33], perturbation theory methods such as iterated perturbation theory [34], local moment approaches [35], and slave-particle approaches [36] etc.

The Kondo lattice regime within the PAM has been investigated heavily by us [35, 37, 38] and the other groups [31, 39, 40] within dynamical mean field theory and cluster extensions ignoring the d - f repulsion effects. We have used local moment approach (LMA) within the DMFT framework previously to understand the PAM in the Kondo lattice (KL) limit [37]. The LMA is a non-perturbative diagrammatic theory based approach developed by Logan and co-workers [41]. This approach has been benchmarked extensively against methods such as Bethe Ansatz [41] and numerical renormalization group [42]. Excellent quantitative agreement has been found, thus providing justification for its use as an impurity solver within DMFT. Further advantages of using LMA are, that real frequency quantities are obtained directly with reasonable computation expense at all temperature and interaction strengths. Our focus in the LMA+DMFT approach to PAM was on universality and scaling in dynamics and transport. A single low energy scale was found to characterize the spectra and transport in the Kondo lattice regime [35]. The mixed-valent regime was not our focus, nevertheless, our studies indicated the absence of universality and scaling, although adiabatic continuity to the non-interacting limit was seen. The dc and optical transport properties were compared to several Kondo insulators and heavy fermion metals and excellent quantitative agreement was found [38, 43]. A few mixed-valent materials such as YbAl_3 and the skutterudite compound $\text{CeOs}_4\text{Sb}_{12}$ were also considered [44] and again good agreement between theory and experiment was found. In a recent work, valence transition in Ytterbium and Europium intermetallics was studied by Zlatić and Freericks [45] employing a multi-component Falicov-Kimball (FK) model within dynamical mean field theory. The authors argue that a complete description would entail a solution of the periodic Anderson model combined with the FK model. However, since this is challenging, they choose to solve just the FK model, albeit a multi-component one. Transport quantities like dc and optical conductivity, thermopower and magnetoresistance etc were calculated and qualitatively compared to the experiment.

Using an equation of motion decoupling approximation, Bennard and Coqblin [46] have investigated the PAM and explored the variation of the f -valence with various parameters of the model. They use the results of this study to understand pressure dependent valence changes. Miyake and co-workers [47] have used a variety of methods including the slave-boson approximation, the density matrix renormalization group etc to investigate the one dimensional extended PAM (EPAM), which includes the $d - f$ repulsion effects represented by U_{cf} . The EPAM has been investigated within dynamical mean field theory by Sugibayashi and Hirashima [48] using quantum Monte-Carlo methods. Their focus has been to understand the interplay between U_{cf} , valence fluctuations and superconductivity. In a recent work Ylvisaker [49] *et. al* combined local density approximation with dynamical mean field theory to understand the valence fluctuation and the valence transition in the Yb metal. For the impurity solver, they have used Hirsh-Fye quantum Monte-Carlo and continuous time quantum Monte-Carlo. They reproduce the experimentally observed valence transition, and conclude that the Yb metal is a fluctuating valence material rather than an intermediate-valent one. As mentioned before and as illustrated through the above mentioned studies, there has been substantial work on the valence transition and its effect on the spectral quantities within the PAM, however the effects on transport quantities due to valence fluctuations and the crossover regime between the Kondo lattice and the mixed-valent regime have received scant attention.

In this work, we focus on such a KL-MV crossover using the LMA+DMFT approach to the PAM. We assume that effects of pressure/doping would be to change the model parameters, and hence a scan of the parameter space within the PAM framework should be able to provide insight into the crossover regime. We highlight the changes occurring in the dynamics and transport properties as a result of this crossover. We find several new results such as a two peak resistivity and anomalous absorption features in the optical conductivity in certain parameter regimes. We provide theoretical explanations for these anomalies, and show that such behaviour does indeed exist in real materials and may be explained quantitatively using the present approach. The paper is structured as follows: We present the model and formalism in the next section. The results and discussions are in sections 3 and 4 respectively. A comprehensive range of experimental measurements is shown to be described by our theoretical results in section 5. We conclude in section 6.

2. Model and Formalism

The periodic Anderson model is one of the simplest models representing a paradigm for understanding the physics of heavy-fermion compounds. In standard notation, the Hamiltonian for PAM is given by

$$\hat{H} = \epsilon_c \sum_{i\sigma} c_{i\sigma}^\dagger c_{i\sigma} - t \sum_{(i,j),\sigma} (c_{i\sigma}^\dagger c_{j\sigma} + \text{h.c.}) + V \sum_{i\sigma} (f_{i\sigma}^\dagger c_{i\sigma} + \text{h.c.})$$

$$+ \sum_{i\sigma} \left(\epsilon_f + \frac{U}{2} f_{i,-\sigma}^\dagger f_{i,-\sigma} \right) f_{i,\sigma}^\dagger f_{i,\sigma} \quad (1)$$

The first two terms describe the c -orbital energy (ϵ_c) and the kinetic energy of the conduction band arising from nearest neighbour hopping t , which is scaled as $t \propto \frac{t^*}{\sqrt{Z_c}}$ (t^* is the unit of energy) in the large dimension limit where the coordination number $Z_c \rightarrow \infty$. We choose the hyper cubic lattice for our calculation, for which the non-interacting density of states given by $\rho_0(\epsilon) = \exp(-\epsilon^2/t_*^2)/t_*\sqrt{\pi}$ is an unbounded Gaussian [26]. The hybridization between the c - and f -electrons is represented by the third term (V) and is responsible for making otherwise localised f -electrons itinerant. The last term is f -orbital site energy (ϵ_f) and the on-site Coulomb repulsion U for two f -electrons of opposite spin.

In the non-interacting ($U = 0$) case, the two orbital energies ϵ_c and ϵ_f completely determine the nature of the ground state, i.e. whether the system would be gapped or gapless at the Fermi level. Equivalently, the occupation numbers $n_f = \sum_\sigma \langle f_{i\sigma}^\dagger f_{i\sigma} \rangle$ and $n_c = \sum_\sigma \langle c_{i\sigma}^\dagger c_{i\sigma} \rangle$ may also be used to characterize the ground state. It is straightforward to see that the system is a band insulator for $n_f + n_c = 2$, while it is metallic for $n_f + n_c \neq 2$ [4]. In the absence of hybridization, i.e. $V = 0$, the f and c sites decouple from each other. Since the f -part is site-diagonal in this limit, the f -Green functions are trivial to obtain, e.g. through the equation of motion method [50]. The tight-binding part along with the on-site c -orbital energy may be solved through Feenberg renormalized perturbation theory (FRPT) [50], and the non-interacting Green's function may be obtained as $g_0^c(\omega) = (\omega^+ - \epsilon_c - S(\omega))^{-1}$. The Feenberg self-energy $S(\omega)$ is in fact a lattice-specific functional of g_0^c ; For example, $S[g_0^c] = \frac{1}{4}t_*^2 g_0^c$ for the Bethe lattice in the limit of infinite dimensions [50].

Within DMFT, the f -selfenergy, $\Sigma(\omega)$ is local [26,27] in real space, hence the FRPT may be used for $V \neq 0$ also to obtain the f and c -Green's functions. These are then given by [35,43]

$$G^f(\omega) = \left[\omega^+ - \epsilon_f - \Sigma(\omega) - \frac{V^2}{\omega^+ - \epsilon_c - S(\omega)} \right]^{-1} \quad (2)$$

$$G^c(\omega) = \left[\omega^+ - \epsilon_c - S(\omega) - \frac{V^2}{\omega^+ - \epsilon_f - \Sigma(\omega)} \right]^{-1} \quad (3)$$

where $\Sigma(\omega)$ is the momentum-independent f -self-energy representing interaction effects and $S(\omega)$ is the same functional of G^c as it is of g_0^c in the non-interacting limit. This Feenberg self-energy may be obtained through the relations given below (please see references [35,43] for more details):

$$G^c(\omega) = H[\gamma] = \int_{-\infty}^{\infty} \frac{\rho_0(\epsilon)}{\gamma(\omega) - \epsilon} = \frac{1}{\gamma(\omega) - S(\omega)} \quad (4)$$

where $H[\gamma]$ denotes the Hilbert transform of γ with respect to the non-interacting density of states $\rho_0(\epsilon)$. While $\gamma = \omega^+$ in the $V = 0$ limit, for finite V , it is given by $\gamma(\omega) = \omega^+ - \epsilon_c - V^2[\omega^+ - \epsilon_f - \Sigma(\omega)]^{-1}$.

2.1. Local moment approach: theory and practice

As mentioned in the introduction, within DMFT, the lattice model is mapped onto an impurity model with a self-consistently determined hybridization. And the solution of the resulting impurity problem is the most challenging step in the solution of the lattice model. We choose the local moment approach within DMFT to solve the PAM. The LMA has been benchmarked extensively in case of the SIAM with other exact methods such as NRG and Bethe Ansatz. While in case of the PAM, excellent agreement with experiments for a wide variety of materials ranging from Kondo insulators to heavy fermion metals and for a range of experiments such as dc and optical transport as well as magnetotransport justifies its use to understand the crossover from Kondo lattice regime to the empty orbital regime via the mixed valence regime. The theoretical formalism and practical implementation are described in references [35,37,43], and the reader is referred to these works for details.

2.2. Transport: linear response

Within DMFT, vertex corrections are absent, hence the single-particle Green's functions are sufficient within Kubo formalism to obtain transport quantities such as dc resistivity and optical conductivity. The expressions derived previously [37] can be brought into a simpler form (derived in the appendix) given below:

$$\sigma(\omega) = \frac{\sigma_0}{2\pi^2} \text{Re} \int_{-\infty}^{\infty} d\omega' \frac{n_F(\omega') - n_F(\omega + \omega')}{\omega} \left[\frac{G^{c*}(\omega') - G^c(\omega + \omega')}{\gamma(\omega + \omega') - \gamma^*(\omega')} - \frac{G^c(\omega') - G^c(\omega + \omega')}{\gamma(\omega + \omega') - \gamma(\omega')} \right] \quad (5)$$

where $\sigma_0 = 4\pi e^2 t^2 a^2 n / \hbar$ for lattice constant a , electronic charge e , and electron density n and $\gamma(\omega) = \omega^+ - \epsilon_c - V^2[\omega^+ - \epsilon_f - \Sigma(\omega)]^{-1}$. The DC conductivity is obtained by considering the $\omega \rightarrow 0$ limit (see appendix for more details) of the above equation as

$$\sigma_{DC} = \frac{\sigma_0}{2\pi^2} \text{Re} \int_{-\infty}^{\infty} d\omega \left(-\frac{dn_F}{d\omega} \right) \left[\frac{\pi D^c(\omega)}{\text{Im}\gamma(\omega)} + 2(1 - \gamma(\omega)G^c(\omega)) \right] \quad (6)$$

where $D^c(\omega) = -\text{Im}G^c(\omega)/\pi$ is the spectral function of the retarded Green's function $G^c(\omega)$ and $n_F(\omega) = (e^{\beta\omega} + 1)^{-1}$ is the Fermi function.

3. Results

In this section, we show results for spectral functions, i.e the density of states (dos), at both zero and finite temperature, optical conductivity again for $T \geq 0$, and DC resistivity. We work with a reasonably large interaction strength ($U \simeq 4.5t_*$) and a hybridization strength of $V^2 = 0.6t_*^2$. The crossover from Kondo lattice regime to the mixed-valent regime is investigated by varying ϵ_c and ϵ_f such that the total occupancy $n_{tot} = n_c + n_f$ is fixed, and n_f is decreased. This is done because pressure experiments would be expected to keep the total occupancy fixed. The practical details of implementation are given in references [35,37]. We begin with the low energy scale and the spectra.

3.1. Coherence scale

The low energy coherence scale has been identified in previous studies to be $\omega_L = ZV^2/t_*$, where $Z = (1 - \partial\Sigma/\partial\omega|_{\omega=0})^{-1}$ is the quasiparticle weight (inverse effective mass). This scale is exponentially small in the strong coupling Kondo lattice regime ($n_f \rightarrow 1$). Spectral functions, optical conductivities and resistivity were shown to be universal functions of $(T/\omega_L, \omega/\omega_L)$ in our previous studies [35,37,43]. Figure 1 shows the variation of the lattice coherence scale ω_L with the f -orbital occupancy n_f for fixed $n_{tot} = 1.25$ (filled circles) and 1.1 (squares). A crossover from the Kondo lattice regime ($n_f \rightarrow 1$) through the mixed-valence regime ($0.3 \lesssim n_f \lesssim 0.8$) to the empty orbital regime ($n_f \ll 1$) manifests in a rapid increase in ω_L . A lowering of the f -orbital

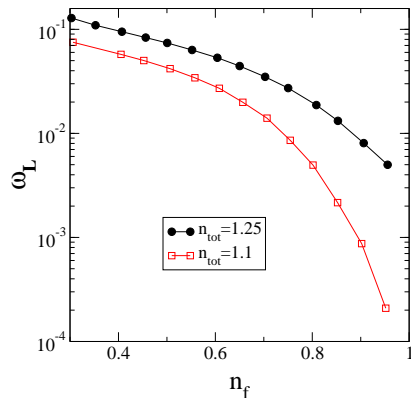


Figure 1. A sharp decrease of the lattice coherence scale, ω_L is seen, with n_f increasing from the empty orbital regime ($n_f \ll 1$) through the mixed-valence regime ($0.3 \lesssim n_f \lesssim 0.8$) to the Kondo lattice regime ($n_f \rightarrow 1$).

occupation implies greater local charge fluctuations, implying an effective decrease of correlation effects. This in turn implies a decrease in effective mass or an increase in Z and hence an increase in ω_L with decreasing n_f .

3.2. Density of states: Zero temperature

The density of states or the spectral functions are considered next. Changes in the low frequency Kondo resonance and in the high frequency Hubbard bands are identified.

We show the $T = 0$ spectral functions ($D^\nu(\omega; T = 0) = -\text{Im}G^\nu(\omega, T = 0)/\pi$ $\nu = f, c$) as a function of the absolute frequency ω/t_* in the left panel of figure 2. In the f -dos (solid line), a usual three peak structure with high energy Hubbard bands and a narrow Kondo resonance at the Fermi level is seen for higher n_f ($\gtrsim 0.7$). For lower n_f , a new spectral feature (marked by an arrow) appears above the Fermi level, the weight of which grows with decreasing n_f . The lower Hubbard band (LHB) moves closer to the Fermi level, while the upper Hubbard band (UHB) shifts to higher energies with decreasing n_f . The middle panel in figure 2 shows the Kondo resonance in greater detail as a function of the scaled frequency ω/ω_L . Close to the Kondo lattice regime, a pseudogap is seen straddling the resonance, which gets progressively filled up and for

the lower values of n_f , there is no trace of a pseudogap. Such a transfer of spectral weight is very non-trivial and is a very significant feature since it manifests clearly in a second peak in optical conductivity, as will be discussed in sections 3.4 and 4.2.

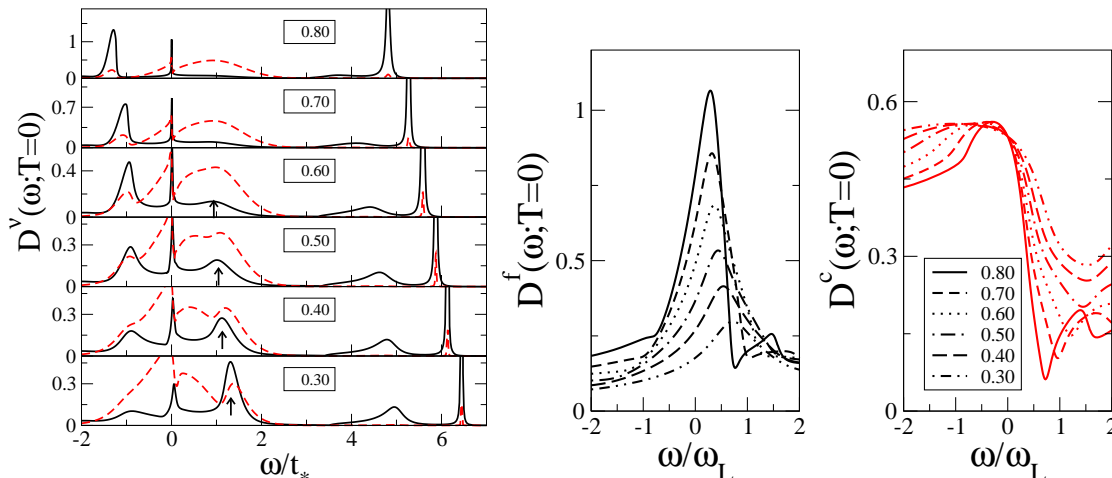


Figure 2. (colour online) Left panel: The zero temperature spectral functions, $D^\nu(\omega; T=0)$, $\nu = c$ (dashed), f (solid) are shown as a function of ‘absolute’ frequency ω/t_* for various f -occupancies (n_f , indicated in the boxes and in the legends) and a fixed $n_{tot} = 1.25$. The middle and the right panels show the same spectra as the left panel, but as a function of the scaled frequency ω/ω_L highlighting the changes in the Kondo resonance and the pseudogap.

The conduction band density of states, $D^c(\omega; T=0)$, shown in the left panel (red dashed lines) of figure 2, has an overall Gaussian envelope, with spectral weight carved out at the effective f -level, ϵ_f^* (seen clearly in the right panel of figure 2 and further discussed in section 4.1) in the form of a pseudogap and small Hubbard bands flanking the envelope. In contrast to the f -dos (left panel of figure 2), the Hubbard bands here possess a very small fraction of the total spectral weight. The lower Hubbard band is distinct from the envelope at higher n_f ($\gtrsim 0.6$), and merges into the envelope at lower n_f ($\lesssim 0.5$). The pseudogap fills up with decreasing n_f and for the lowest n_f values shown, there is indeed no trace of a pseudogap (see inset). The position of the Kondo resonance, the Hubbard bands and a few other aspects are discussed in greater detail in subsection 4.1.

3.3. Density of states: Temperature dependence

In figure 3, we show the evolution of the f -dos as a function of temperature for $n_f = 0.8$ and $n_f = 0.3$ in the left and right panels respectively. The insets in the panels show the low frequency, low temperature ($(\omega/\omega_L, T/\omega_L) \sim \mathcal{O}(1)$) part more clearly.

The left inset shows that the pseudogap proximal to the Fermi level fills up, while a thermal broadening of the Kondo resonance is clearly visible in the f -dos. At any given temperature T , it is expected that changes in the spectral function will occur in the frequency range $\omega \lesssim T$. And indeed, this is seen in the KL regime as discussed

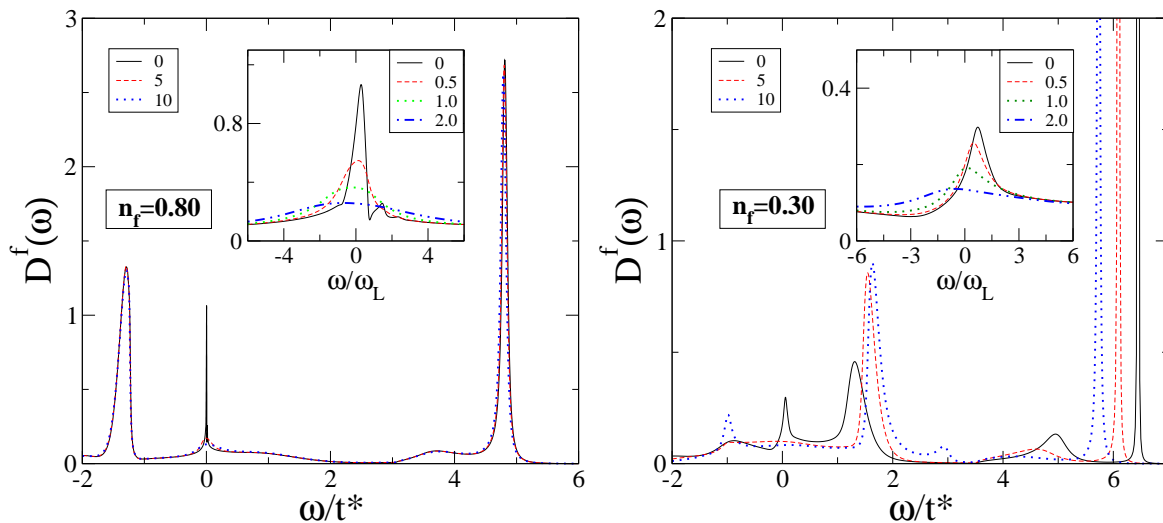


Figure 3. The f -electron spectral function at temperatures $\tilde{T} = T/\omega_L = 0, 2, 5, 10, 20$ (indicated in legends) and for all scales in the main panel. The insets show the low frequency part as a function of scaled frequency for lower temperatures. The left panel is for $n_f = 0.80$ and the right panel is for $n_f = 0.30$ (with fixed $n_{tot} = 1.25$).

below and in reference [37]. The main left panel shows spectra for three different temperatures, which are hard to distinguish. This implies that there has hardly been any spectral weight transfer on a scale of t_* , even at the highest temperature shown ($\tilde{T} = 10$, equivalent to $\sim 0.18t_*$).

The physics in the mixed-valent regime is, naturally, different. The coherence scale is not exponentially small (see figure 1). In this regime, spectral weight transfer occurs in an energy interval that is far greater than the thermal energy scale. This may be seen in the right panel of figure 3, where at a temperature of $5\omega_L$ ($\sim 0.77t_*$), the UHB which is at $\sim 6t_*$ and hence about 15 times the temperature gets strongly affected. In fact, the integrated spectral weight in the UHB is found to decrease with T . Such differences in terms of spectral weight transfer between the KL and MV regime have been noted previously [37]. The new spectral feature above the Fermi level (marked by an arrow in the left panel of figure 2) that emerges distinctly in the MV regime gains spectral weight and grows with increasing T . The reason for the growth of this feature is not completely clear; however, since the total spectral weight is conserved, the melting of Kondo resonance and the loss of spectral weight in the UHB with increasing T must be compensated by gain in spectral weight elsewhere, and this could be one of the reasons for the growth of this feature with increasing T .

Angle-resolved photoemission experiments should be able to easily identify such a feature. The conduction band density of states exhibits similar temperature dependence as the f -dos and is hence not shown.

3.4. $T = 0$ optical conductivity

As mentioned before, the zero temperature Green's functions are sufficient within DMFT to compute the $T = 0$ optical conductivity, $\sigma(\omega; T = 0)$ (equations 5) [26,27]. In figure 4, we show $\sigma(\omega; T = 0)$ as a function of frequency (ω/t_*) for various values of n_f and a fixed $n_{tot} = 1.1$. For $n_f \rightarrow 1$, a familiar structure of a single mid-infrared peak (MIR) arising due to interband transitions [51], marked with a thin dashed arrow in figure 4, is obtained. As we decrease n_f , the MIR peak shifts to higher frequencies. A Drude peak is obtained at the lower frequencies for all n_f , but it cannot be shown here since it is a Dirac delta function for $T = 0$.

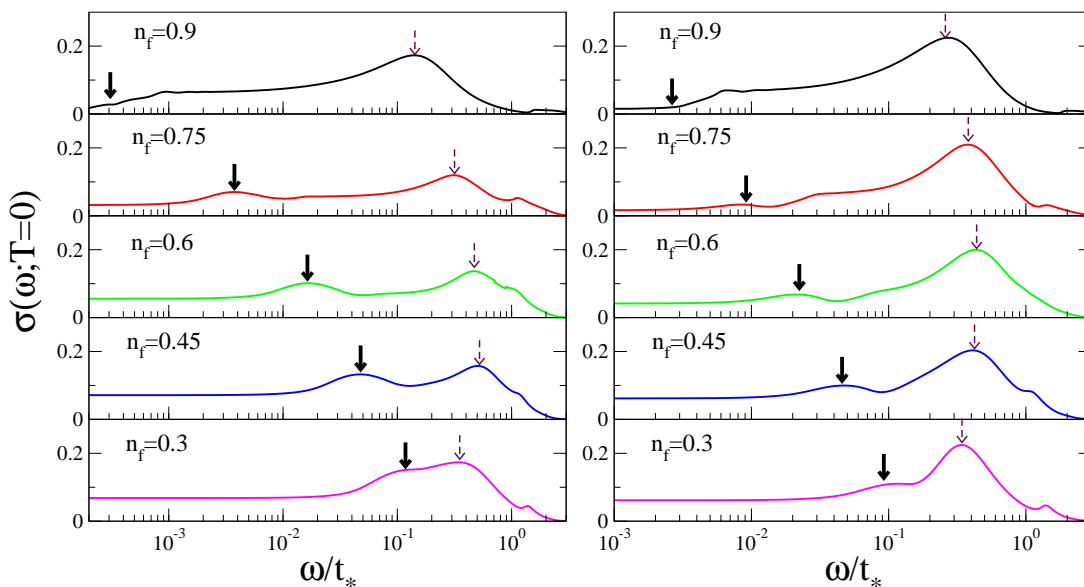


Figure 4. The zero temperature optical conductivity $\sigma(\omega; T = 0)$ as a function of frequency (ω/t_*) for various n_f , and fixed $n_{tot} = 1.1$ (left panel) and 1.25 (right panel). The MIR peak is marked with a thin dashed arrow, while the DMIR feature is marked with a thick solid arrow.

The lower n_f values hold a surprise. A deep mid-infrared (DMIR) absorption feature or a shoulder, marked with a thick solid arrow in figure 4, emerges for lower n_f values. This is distinct from the above mentioned MIR peak. Such a two peak structure has been reported earlier for the classic mixed valent compound CePd_3 [52] and recently for YbIr_2Si_2 [12]. For the former compound, spin-orbit splitting was argued to be responsible for the two peaks, but the latter has not been understood quantitatively. Recently it has been pointed out through band structure studies that the DMIR feature could be due to transitions to the effective f -level [53]. Here we confirm that this feature could indeed arise from absorption into the effective f -level at $\epsilon_f^* = Z(\epsilon_f + \Sigma(0))$, at which frequency, a pseudogap appears in the spectral functions (figure 2). Thus the scenario proposed here could be relevant for both CePd_3 and YbIr_2Si_2 . A detailed discussion of the effective f -level, the pseudogap and transfer of spectral weight into the pseudogap region is given in section 4.2.

Here we must add that a two-peak structure is indeed obtained for higher n_{tot} , such as $n_{tot} = 1.25$ shown in the right panel of figure 4 and hence is a generic feature in the crossover regime. Furthermore, with decreasing n_f , the DMIR feature merges into the MIR peak, without being able to develop into a full distinct peak for lower n_f , and hence gets harder to distinguish for higher n_{tot} .

We now move on to finite temperature transport.

3.5. DC Resistivity as a function of temperature

In figure 5, we show the dc resistivity as a function of temperature T/t_* . The left panel shows the resistivity for $0.65 \leq n_f \leq 0.95$, while the right panel is for $0.30 \leq n_f \leq 0.60$. The theoretically computed $\rho(T)$ all have zero residual values, but for visual clarity, they have been appropriately vertically offset (mentioned in the caption). There is a clear shift of the coherence peak (low temperature peak) to higher temperatures since its position correlates with the low energy scale [37], and ω_L itself increases sharply with decreasing n_f . For $n_f \lesssim 0.8$, a second maximum begins to form at higher temperature. This second peak become easily distinguishable in the mixed-valence regime and merges into the coherence peak to yield a broad maximum close to the empty orbital regime (see right panel, $n_f \lesssim 0.45$). Here we have shown that the crossover from the Kondo lattice

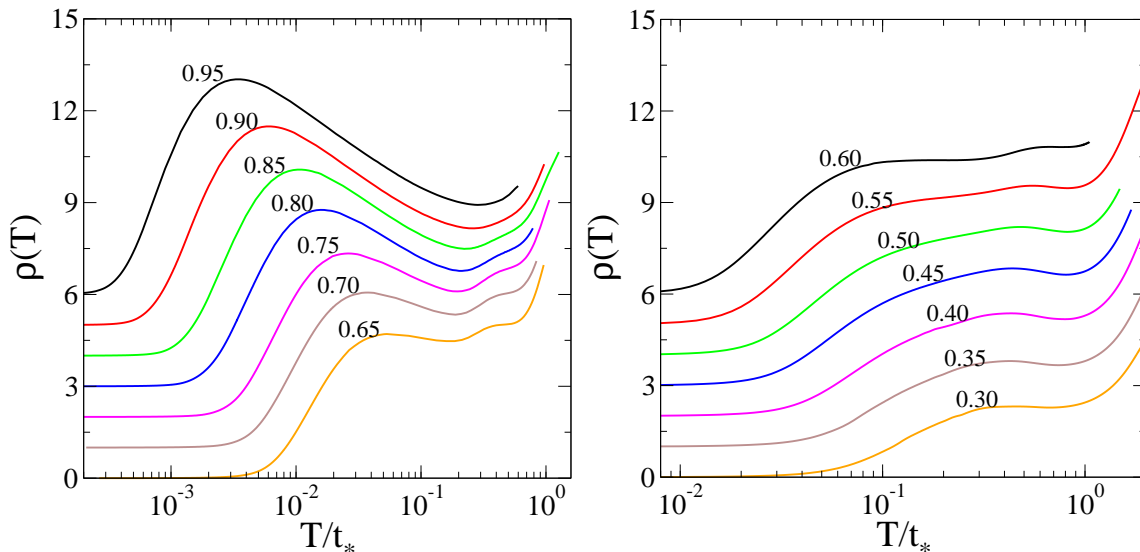


Figure 5. DC resistivity for various n_f values (mentioned next to the curve) as a function of temperature T/t_* for a fixed $n_{tot} = 1.25$. The theoretically computed $\rho(T)$ all have zero residual values, but for visual clarity, they have been appropriately vertically offset. For example - in the left panel, we add a temperature independent ρ_0 that is zero for $n_f = 0.65$ and increases by unity for every higher n_f ($\rho_0 = 1, 2, 3, \dots$ for $n_f = 0.7, 0.75, 0.8, \dots$).

regime to the mixed-valent regime involves the coalescing of the coherence peak and a high temperature peak into a single broad peak. This high temperature peak is not present in the KL regime or the empty orbital regime, and appears in the mixed-valent

regime only due to the proximity of the Hubbard band to the Fermi level (discussed in detail in section 4.3). Although we have displayed data in figure 5 for $n_{tot} = 1.25$, the two peak structure is a generic feature of the mixed-valent regime for other n_{tot} as well. However, the degree to which the two peaks can be distinguished and identified varies in different parameter regimes.

Pressure/doping-dependent resistivity measurements in CeCu_2Si_2 [8, 9, 20] show similar behaviour. For low pressure, a two peak resistivity is observed. As a function of increasing pressure, the two peaks merge and a single broad peak is seen. In the experimental paper, the effect of pressure was ascribed to a crossover from Kondo lattice to intermediate valence, however the second peak was argued to arise from higher lying crystal-field multiplets. Here, although we do concur with the crossover phenomenon, we present an alternative scenario for a two peak resistivity structure. The scenario is that with increasing pressure, the valence decreases, bringing the Hubbard band in the proximity of the Fermi level, thus leading to a second peak arising due to the Hubbard band states contribution. We emphasise here that a two-peak structure is obtained in our theory despite the model Hamiltonian (equation 1) not containing crystal-field effects.

We now move on to finite temperature optical transport.

3.6. $T > 0$ Optical transport

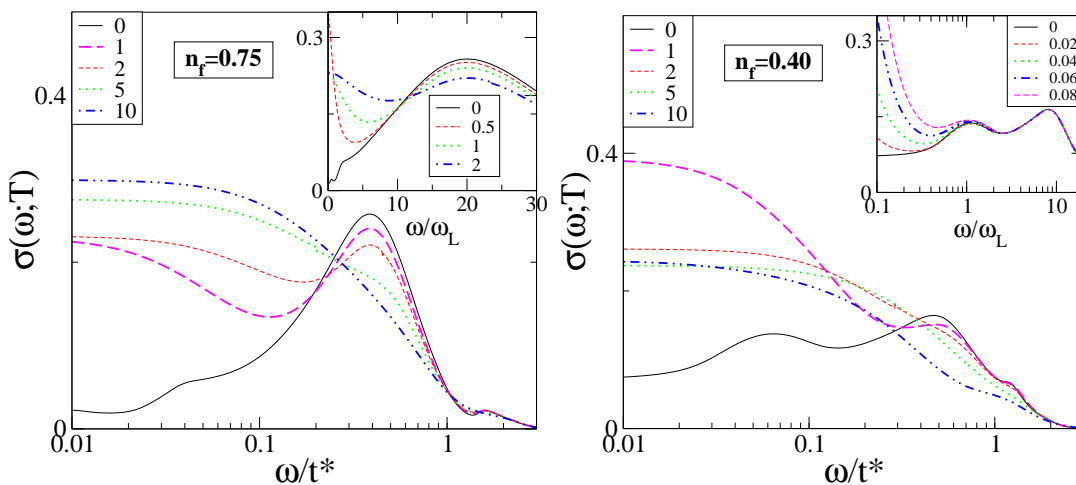


Figure 6. Optical conductivity $\sigma(\omega; T)$ for $n_f = 0.75, n_c = 0.61$ and $n_f = 0.40, n_c = 0.71$ in the left and right panels respectively ($\epsilon_c = 0.5t_*$ and $U \sim 4.7t_*$) as a function of ω/t_* in the main panels and as a function of ω/ω_L in the insets respectively for various temperature values (given as multiples of ω_L in the legends). The insets show $\sigma(\omega; T)$ for low temperatures to show the transfer of spectral weight more clearly.

We now show the temperature dependence of the optical conductivity in figure 6 for two different f -occupancies, 0.75 and 0.4 (other parameters are mentioned in the figure caption) in the left and right panels respectively. The $\sigma(\omega; T)$ for the higher n_f case has a usual prominent mid-infrared (MIR) peak, with a slight shoulder at lower

frequencies. The inset shows the low temperature evolution of $\sigma(\omega)$, while the main panel shows $T \leq 10\omega_L$. With increasing temperature, a transfer of spectral weight over all energy scales is seen. The lower $n_f(0.4)$ optical conductivity shown in the right panel of figure 6 is qualitatively different from that of the left panel. The shoulder like structure seen in the Kondo lattice regime (left panel) develops into a full peak in the mixed-valent regime, while the MIR peak diminishes in intensity and gets broader. The analysis at $T = 0$ shows (see section 4) that the lower frequency peak occurs at the effective f -level ϵ_f^* . The inset shows that the DMIR peak or the shoulder appears only below a temperature $T = 0.08\omega_L$ even though it is positioned at a frequency ω equal to the coherence scale ω_L (since here $\epsilon_f + \Sigma(0) \sim 1$). This precise behaviour is seen in recent optical conductivity measurements in YbIr_2Si_2 [12](see section 5).

4. Discussion

4.1. Spectral features: Kondo resonance and Hubbard bands

In this subsection, we discuss the positions and weights of the various features seen in the spectra in section 3.2. At high energies, the prominent spectral features are the Hubbard bands. In figure 2, it is seen that the Hubbard bands shift to the right with decreasing n_f . This is expected from the atomic limit, since in that limit, the Hubbard bands occur at ϵ_f and $\epsilon_f + U$, and ϵ_f moves closer to the Fermi level when n_f decreases. However, we find from our calculations, that in the displayed spectra, the Hubbard bands are not at the positions predicted by the atomic limit, as must be expected, due to a combination of shifts in the levels arising through hybridization and self-energy effects. We see that even for $n_f \sim 0.8$, the LHB and the UHB are not symmetrically placed about the Fermi level as would have been the case in the strong coupling KL regime. In fact, the LHB is at $\omega \lesssim -t_*$, while the UHB is at $\omega \gtrsim U$. The LHB is predicted very well by the unrestricted Hartree Fock (UHF) solution (not discussed here) which considers the static part of the self energy and hybridization effects. For predicting the UHB, we can neglect hybridization effects, however, we need to retain the static part and *most importantly* the real part of the self energy. The latter may be approximated by an expression obtained through high frequency moment expansion [54], and thus the UHB turns out to be at $\sim (\bar{\epsilon}_f + \sqrt{\bar{\epsilon}_f^2 + \bar{U}^2})/2$, where $\bar{\epsilon}_f = \epsilon_f + U(\bar{n} + \bar{\mu})/2$, $\bar{U}^2 = U^2\bar{n}(2 - \bar{n})$ and $\bar{n}, \bar{\mu}$ have been defined in section 4.2 of reference [35] as the fictitious occupation number and the moment obtained from the spin-dependent host/medium propagators that are used to construct the LMA self-energies.

In the other extreme, i.e close to the Fermi level, a low frequency form of the Green's functions using a Fermi liquid self-energy $\Sigma(\omega) = \Sigma(0) + \omega(\frac{1}{2} - 1) + \mathcal{O}(\omega^2)$ may be derived that enables us to understand most of the features of the Kondo resonance. The resulting spectral functions in the neighbourhood of the Fermi level are given by

$$D^c(\omega) \sim \rho_0 \left(\omega - \epsilon_c - \frac{ZV^2}{\omega - Z\bar{\epsilon}_f} \right)$$

$$V^2 D^f(\omega) \sim \left(\frac{ZV^2}{\omega - Z\bar{\epsilon}_f} \right)^2 D^c(\omega) \quad (7)$$

where $\epsilon_f^* = Z\bar{\epsilon}_f = Z(\epsilon_f + \Sigma(0))$ is the effective f -level. These equations show that the low energy ($\omega \lesssim \omega_L$) spectral features are precisely those of a non-interacting ($U = 0$) PAM with renormalized parameters ($V^2 \rightarrow ZV^2, \epsilon_f \rightarrow Z(\epsilon_f + \Sigma(0))$ and ($\epsilon_c \rightarrow \epsilon_c$) [35]. Thus, this is the renormalized non-interacting limit (RNIL). A scaling collapse of the numerically obtained spectra with the analytical expressions above would be a demonstration of adiabatic continuity of the interacting system to the non-interacting limit. Indeed, we do see such a collapse (not shown), implying adiabatic continuity, although the range of frequencies over which such a collapse occurs decreases from $\omega \lesssim \omega_L$ in the KL regime, to $\omega \ll \omega_L$ in the empty orbital regime.

As $\omega \rightarrow \epsilon_f^*$ in equations 7, the renormalized non-interacting limit spectral functions also vanish, thus the pseudogap seen in the spectra is positioned at the effective f -level, $\epsilon_f^* = Z(\epsilon_f + \Sigma(0))$. Transfer of spectral weight into the pseudogap happens with decreasing n_f as seen in figure 2 which implies that the frequency interval in the neighbourhood of ϵ_f^* is gaining spectral weight. This spectral weight transfer is completely missed by theories that are equivalent to the renormalized non-interacting limit. This includes approaches such as slave-boson theories or two-band models of heavy fermion systems, which ignore the imaginary part of self-energy. The variation of ϵ_f^* with n_f may be easily predicted using the Luttinger's theorem which states [35]

$$\frac{1}{2}(n_f + n_c) = \int_{-\infty}^{-\epsilon_c + V^2/\bar{\epsilon}_f} \rho_0(\epsilon) d\epsilon + \theta(-\bar{\epsilon}_f). \quad (8)$$

For fixed $n_{tot} = n_f + n_c$, the upper limit of integration on the right side of equation 8 is also fixed. Crossing over from the KL to MV regime would require decreasing n_f and increasing n_c , which in turn would require decreasing ϵ_c . Thus to keep $-\epsilon_c + V^2/\bar{\epsilon}_f$ fixed, the $\bar{\epsilon}_f = \epsilon_f + \Sigma(0)$ must increase, and hence the effective f -level, $\epsilon_f^* = Z\bar{\epsilon}_f$, also increases as n_f decreases. This is indeed seen in the figure 2 because the position of the pseudogap does indeed shift to higher frequencies as n_f is decreased.

4.2. Inadequacy of the renormalized non-interacting limit

In [37], it was shown that the two band model or the RNIL predicts a square root singularity at the minimum direct gap ($\sim 2\sqrt{Z}V$), and hence the MIR peak is generally attributed to the direct gap. A simple Fermi-liquid analysis $\Sigma(\omega) \simeq \text{Re}\Sigma(0) + \omega(1 - 1/Z)$ of the poles of the \mathbf{k} -dependent conduction electron Green's function

$$G^c(\omega; \epsilon_{\mathbf{k}}) = \left[\omega^+ - \epsilon_c - \epsilon_{\mathbf{k}} - \frac{V^2}{\omega^+ - \epsilon_f - \Sigma(\omega)} \right] \quad (9)$$

yields a two-band model

$$\omega_{\pm}(\epsilon_{\mathbf{k}}) = \frac{(\epsilon_c + \epsilon_{\mathbf{k}} - \epsilon_f^*) \pm \sqrt{(\epsilon_c + \epsilon_{\mathbf{k}} - \epsilon_f^*)^2 + 4ZV^2}}{2} \quad (10)$$

The minimum direct gap is given by $\min(\omega_+(\epsilon_{\mathbf{k}}) - \omega_-(\epsilon_{\mathbf{k}}))$. The square root singularity at the direct gap appears in the two band model because the imaginary part of the self energy is neglected, and the resulting spectral functions are Dirac delta functions. Including incoherent effects due to electron-electron scattering results in broadening of the MIR peak and cutting off the square root singularity.

At the lowest n_f values, a clear two-peak structure is visible in the optical conductivity displayed in the figure 4 (especially for $n_f = 0.45$ in the left panel). The low frequency peak is in fact at the effective f -level, as argued below, while the high frequency peak is the usual MIR peak. Naively, finding an absorption peak at ϵ_f^* is counter-intuitive, because the renormalized non-interacting limit (equations 7) shows that a pseudogap exists at ϵ_f^* , implying that there is no density of states at that energy. So how can absorption into a gap happen? The answer is of course that the RNIL, which is equivalent to a slave-boson mean-field theory, which in turn is equivalent to a two-band model [51], are not totally correct in their predictions. These approaches neglect the imaginary part of the self-energy (scattering rate). So even though the RNIL predicts a gap, there is in fact no gap at ϵ_f^* when self-energy effects are included (see the pseudogap feature in the density of states in figure 2, and the discussion in section 4.1). And in fact, it may be shown rigorously, without recourse to LMA that absorption to ϵ_f^* will happen provided the imaginary part of self energy is non-zero at that energy. To see this, consider the roots of the real part of the denominator of the conduction electron Green function, $G^c(\omega, \epsilon_{\mathbf{k}})$ (equation 9), given by

$$\begin{aligned} \text{Re} [\omega - \epsilon_c - \epsilon_{\mathbf{k}} - V^2 (\omega - \epsilon_f - \Sigma(\omega))^{-1}] = \\ \omega - \epsilon_c - V^2 \frac{\omega - \epsilon_f - \text{Re}\Sigma(\omega)}{(\omega - \epsilon_f - \text{Re}\Sigma(\omega))^2 + (\text{Im}\Sigma(\omega))^2} = \epsilon_{\mathbf{k}} \end{aligned} \quad (11)$$

If the imaginary part of the self energy is completely neglected and a first order Taylor expansion is carried out for the real part of the self energy, we get back equation 10. However, retaining the imaginary part, however small it might be, results in an equation that is at least cubic in order. And for $\epsilon_{\mathbf{k}} = \epsilon_c - Z(\epsilon_f + \Sigma(0))$, one of the roots is just $\epsilon_f^* = Z(\epsilon_f + \Sigma(0))$.

We support the arguments above with LMA results below. The dispersion, $\omega(\epsilon_{\mathbf{k}})$ is computed for $n_f = 0.95(n_c = 0.58)$, $0.7(n_c = 0.63)$ and $n_f = 0.4(n_c = 0.71)$ with $\epsilon_c = 0.5$, $U \sim 4.7t_*$ through equation 11 and shown in the top, middle and bottom panels respectively in figure 7. The two-bands obtained at the renormalized non-interacting level (eq. 10) are also superimposed in red. It is clear from the figure that the agreement of the two-band model with the full dispersion gets progressively worse as n_f decreases. For $n_f = 0.4$, the middle band is clearly visible in the full dispersion, while being completely absent in the two-band picture. This third band, as argued above is centred at $\omega = \epsilon_f^*$. It is the excitations from the ‘band’ below the Fermi level to ϵ_f^* , that appears as an additional ‘anomalous’ absorption peak in the deep mid-infrared region (as a shoulder). This anomalous peak is seen to become prominent in the mixed-valent regime and is very small or invisible in the Kondo lattice regime. We refer the reader

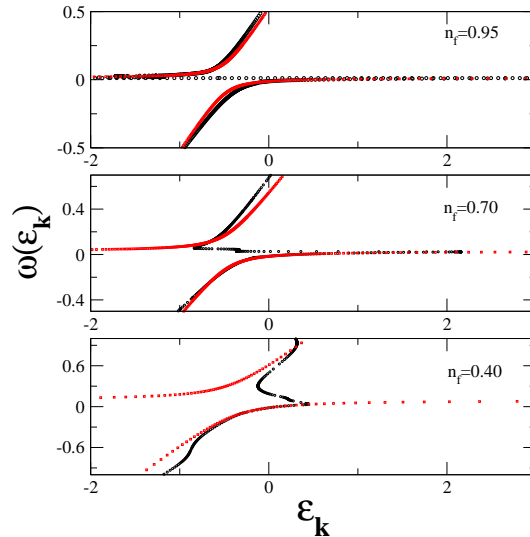


Figure 7. The dispersion $\omega(\epsilon_{\mathbf{k}})$ computed from equation 11 (black) and from the RNIL, equation 10 (red) for $\epsilon_c = 0.5t_*$, $U \sim 4.7t_*$ and $n_f = 0.95, n_c = 0.58$ (top panel), $n_f = 0.70, n_c = 0.63$ (middle panel) and $n_f = 0.40, n_c = 0.71$ (bottom panel).

to figure 4, where an extra absorption feature is easily discernible for lower n_f values, while for higher n_f values, just a weak shoulder is observed. As we will see later, such a two-peak optical conductivity has indeed been observed in recent experiments (section 5).

4.3. Two-peak resistivity: why?

We have shown previously that the coherence peak (low temperature peak) in the resistivity, which would be a minimum in the conductivity [37], occurs at a temperature comparable to ω_L , the low temperature scale. A second peak (high temperature peak) has indeed been observed in experiments and has been attributed to crystal field split levels (for example in Ref [8]). Notwithstanding the foregoing possibility, we find an alternative and far simpler explanation for the existence of the second peak even within the single band PAM. The second peak occurs at a temperature that is roughly half of the lower Hubbard band energy scale. It might at first seem surprising to note that the Hubbard band is contributing to transport. The Hubbard bands are usually at an energy scale of $U/2$ in the strong coupling Kondo lattice regime which being of the order of a few eV, remain untouched until room temperature. Nevertheless, for mixed-valent systems, even if the U is large, either the LHB or the UHB moves close enough to the Fermi level so as to be affected at room temperature scales.

To show the contribution of the Hubbard band states to the conductivity, we consider expression 6 again. On the right hand side, the integration is carried out over all frequencies. However, if we introduce an upper and a lower cutoff in the integration limits, we can isolate the contribution of individual spectral features within those limits. In figure 8, we show the calculated dc resistivity for $n_f = 0.6, n_c = 0.65$ (same as that in

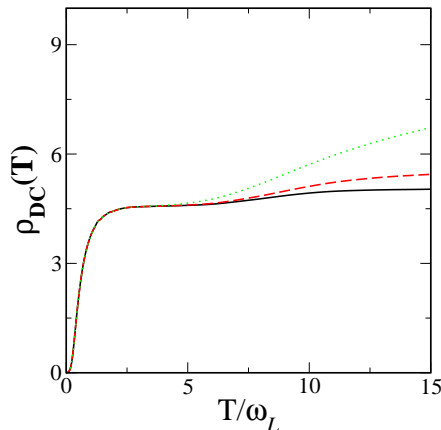


Figure 8. Figure shows that the second peak in the DC resistivity seen most clearly in the right panel of figure 5 for $n_f = 0.6$ disappears progressively by excluding the lower Hubbard band and other spectral features. The solid line is for $n_f = 0.6, n_c = 0.66$ and is the full resistivity. The dashed and the dotted lines are obtained by excluding the lower Hubbard band below the Fermi level and with decreasing cutoff above the Fermi level (see text for discussion).

figure 5), with three different cutoffs: (i) the solid line being no cutoff (full resistivity), (ii) the dashed line having limits such that the lower Hubbard band is excluded but the new ‘non-Hubbard band’ feature above the Fermi level (marked with an arrow in figure 2) is included and (iii) the dotted line having limits such that both the LHB and the new feature is excluded. It is seen that excluding the spectral weight of the Hubbard band and the new feature enhances the resistivity systematically. This shows that the Hubbard band contribution to the dc conductivity is substantial in mixed-valent compounds. The two-peak behaviour of resistivity, is not specific to the parameter regime for which the dc resistivity has been displayed ($U/V^2 \sim 8, n_{tot} = 1.25$). In other parameter regimes, such as $n_{tot} = 1.1$, our calculations demonstrate (not shown here) that the dc resistivity crosses over from a single sharp coherence peak to a broad peak lineshape with decreasing valence, going via a two-peak structure but with very faint or hard to distinguish features.

5. Comparison to Experiments

5.1. DC resistivity: ambient pressure

In figure 9, we have superposed theoretically computed dc resistivity (solid lines) with the experiments (circles) for CeRhIn₅ [55], Ce₂Ni₃Si₅ [56], CeFeGe₃ [57] and YbIr₂Si₂ [12]. To find the appropriate theoretical parameters for each material, we had to adopt a trial and error approach. However, a surprising similarity in the dc resistivity of CeRhIn₅ and Ce₂Ni₃Si₅ reduced our effort substantially. We found that we could take the experimentally measured dc resistivity for the two materials and scale them onto each other simply by rescaling the x and y axes. CeRhIn₅

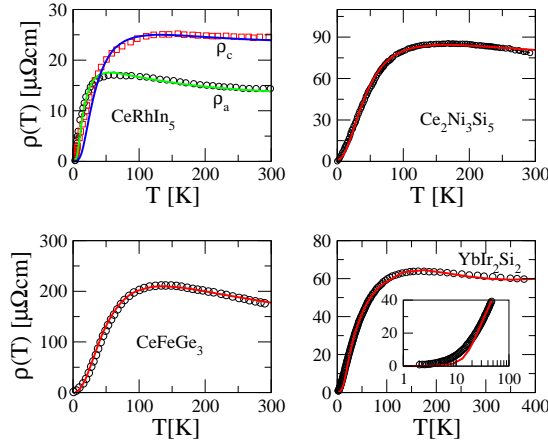


Figure 9. Comparison of resistivity measurements for four different materials with theory. Please refer to text for discussion.

has anisotropic resistivity, nevertheless the ρ_a and ρ_c may also be scaled onto each other, thus showing that qualitatively, they are also similar. We find that these two materials have an f -occupancy $n_f \sim 0.7$, with the rest of the parameters being $n_c \sim 0.55, U/V^2 \sim 8, \epsilon_c = 0.5t_*$. For CeFeGe_3 , we found that the mixed-valence resistivities do not fit the data well. Rather, the best fit was found using parameters ($n_f \sim 1, n_c \sim 0.77, U/V^2 \sim 5, \epsilon_c = 0.3$) that signify an intermediate correlation with f -occupancy being nearly unity. The optical transport data for YbIr_2Si_2 (see below) shows a two-peak structure very similar to that seen in figure 4 for $n_f = 0.4$ and $n_{tot} = 1.1$. Thus we take the same resistivity and superimpose that onto the experimentally measured one, and we see very good agreement.

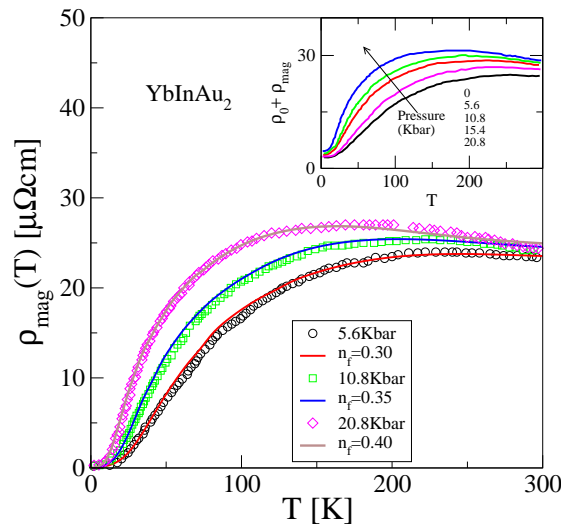


Figure 10. Comparison of pressure dependent resistivity measurements (magnetic contribution only) for YbInAu_2 with theory. The inset shows the reported [58] experimental data.

5.2. DC resistivity: Pressure dependence

Hydrostatic pressure dependence measurements of the dc resistivity of YbInAu_2 and its non-magnetic homologue LuInAu_2 have been carried out by Fuse et.al [58]. The experimental magnetic resistivity along with the residual resistivity ($\rho_{mag} + \rho_0$) is shown in the inset of figure 10. The main panel shows a comparison of theory (solid lines, $n_{tot} = 1.1, U/V^2 \sim 8$) with experiment (symbols). The agreement is seen to be excellent. The T_{max} is seen to decrease with pressure, and the material appears to be progressing towards a Yb^{3+} state with increasing pressure, as conjectured in the experimental paper. Nevertheless, the valence remains in the mixed-valent regime ($\lesssim 0.4$), even with pressures upto 20KBar.

We now move on to CeCu_6 , which has gathered a lot of attention in the past decade as a material that can be tuned to a quantum critical point with Au doping. Pressure dependent resistivity measurements on CeCu_6 were carried out in 1985 by Thompson and Fisk [59]. They found that with increasing pressure, the material crosses over from Kondo lattice like to mixed-valence like regime. In the left panel of figure 11, we show the experimental graph, while in the right panel, the theory (same data as that for figure 5) is shown. The experiment shows that with increasing pressure, the temperature dependence follows the $P = 0$ curve to some temperature and then deviates. In the inset of the left panel, the experimental data for $0 \leq P \leq 17.4\text{kbar}$ is shown to collapse when plotted as R/R_{max} vs. T/T_{max} for $T \leq 4T_{max}$. The theoretical curves in the right panel correspond very closely to those seen in the experiment. The agreement between theory and experiment shows that indeed with increasing pressure, the occupancy does change from $n_f \rightarrow 1$ to $n_f \sim 0.75$, thus implying that the valence of Ce changes from $\sim 3+$ to $\sim 2.75+$. The theory curves decrease more rapidly (than experiment) with increasing temperature beyond the coherence peak, and the reason for this is that the phonon contribution is not subtracted in the experiment. The inset in the theory panel has five different valencies plotted together, namely, $n_f = 0.90, 0.85, 0.80, 0.78$ and 0.75 . Except for $n_f = 0.75$, the rest of the data is seen to collapse onto a single curve, as seen in the experiment. The $n_f = 0.75$ curve does collapse upto a certain temperature and then deviates from the universal curve.

5.3. Optical transport: YbIr_2Si_2

The recently discovered heavy fermion system YbIr_2Si_2 [60] has a crystal structure similar to the well studied YbRh_2Si_2 . The latter exhibits a field-tuned quantum critical point (QCP), while the former has a pressure-tuned first order phase transition to a ferromagnetic phase. The experimentally measured optical conductivity [12] is shown in the top panel of figure 12. A clear two peak structure is evident, and a large scale spectral weight transfer occurs as temperature is increased from 0.4K to 300K. An important characteristic of the temperature dependence of $\sigma(\omega; T)$ is that, as temperature is increased, the lower frequency peak (shoulder) merges into the continuum at $T \sim 60\text{K}$, at which temperature the higher frequency peak remains untouched.

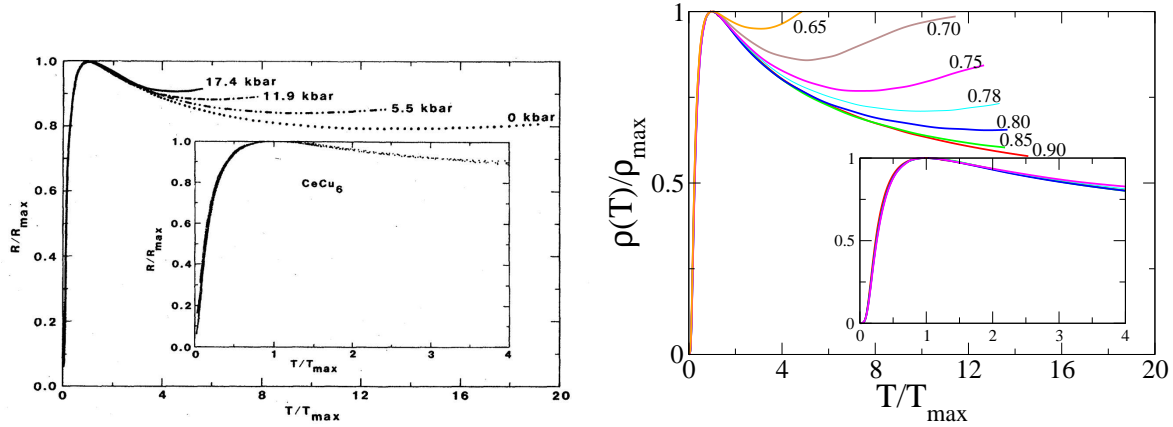


Figure 11. Left panel: Experimentally measured pressure dependent resistivity measurements for CeCu_6 [59]. Right panel: Theoretically computed $\rho(T)$ (same data as left panel of figure 5) plotted as ρ/ρ_{max} vs. T/T_{max} . The respective valencies are mentioned next to the curves.

We note that the theoretically computed optical conductivity shown in figure 6 does appear to resemble the experimentally measured $\sigma(\omega; T)$. In the experiment, the shoulder peak appears only for $T \lesssim 30K$, which, according to theory, should be roughly 0.08 times the peak frequency for the chosen parameters (see the discussion for figure 6). Thus, theoretically, we can predict that the shoulder should appear at $\sim 30.0/0.08K \simeq 32meV$. The shoulder peak position as predicted by theory indeed agrees very well with the experimentally observed shoulder position ($\sim 30meV$). The bottom panel of the same figure shows the optical conductivity computed for $U/t_* \sim 5$, $V^2 \sim 0.6t_*^2$ and $\epsilon_c = 0.5t_*$, which yields $n_f = 0.4$ and $n_c = 0.7$, thus classifying YbIr_2Si_2 as a mixed-valent material. These parameters were chosen using the results shown in figure 4, and for consistency, we note that the dc resistivity in the experiment has a broad and shallow peak (see bottom right panel of figure 9) which indicates that YbIr_2Si_2 belongs to the mixed-valent regime. The DC conductivity obtained through a low frequency limit in the theory is higher than the corresponding experimental values. This is natural, since the theory neglects electron-phonon scattering, which if included would reduce the theoretical conductivities. Apart from this disagreement, an excellent agreement between theory and experiment is seen in quantitative terms for both the lineshape and the temperature dependence. A phenomenological analysis [12] of the experimental optical conductivity using Drude and extended Drude formalism has been used to infer non-Fermi liquid nature of the quasiparticles in this material. However, if the quantitative agreement between theory and experiment is any indication, this material is a perfect Fermi liquid. The self energy has the correct Fermi liquid form for the parameters used to compute the optical conductivity in the bottom panel of figure 12. In our approach, the Luttinger's theorem is used as a constraint, which also supports the inference of Fermi liquid behaviour. The low temperature resistivity also exhibits a clean T^2 behaviour, both in the experiment [13] and theory (shown to

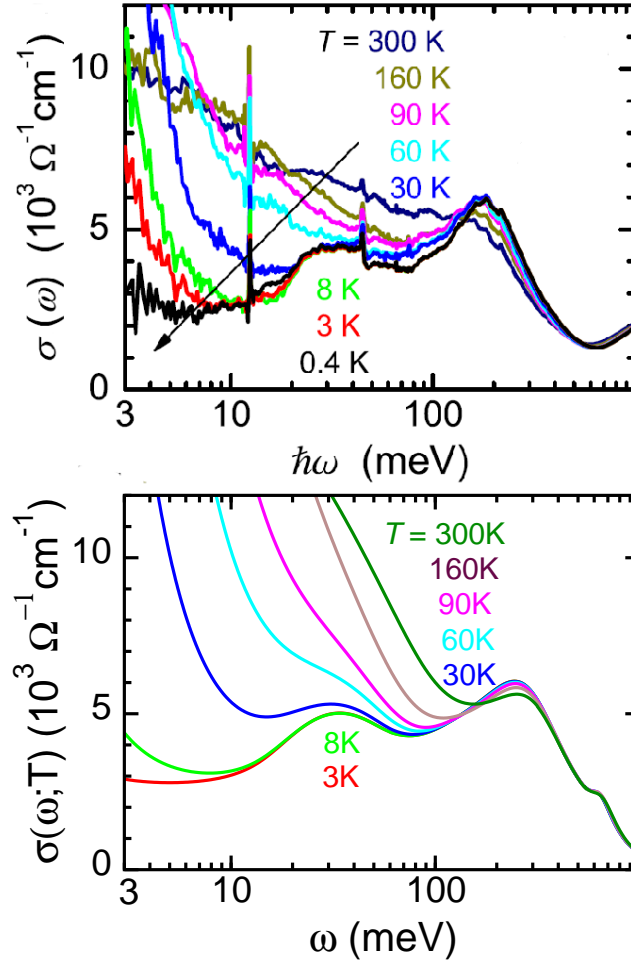


Figure 12. top panel: Experimentally measured optical conductivity for YbIr_2Si_2 . [12] Bottom panel: Theoretically computed $\sigma(\omega; T)$ for $U/t_* \sim 5, V^2 \sim 0.6t_*^2$ and $\epsilon_c = 0.5t_*$, which yields $n_f = 0.4$ and $n_c = 0.7$. Excellent quantitative agreement is observed between theory and experiment for the line shape and the temperature dependence.

agree well in the inset of the bottom right panel in figure 9), which again supports a Fermi liquid ground state. Additionally, we conclude that this material is in the mixed-valent regime with an effective f -occupancy of $n_f = 0.4$, which would correspond to an effective valence $\text{Yb}^{2.4+}$. (Naturally, the n_f given here must be interpreted as hole occupancy for Yb compounds.) This effective valence predicted by our theory disagrees with the inference from susceptibility measurements, which yields a Yb valence close to $3+$. Further theoretical and experimental investigations are needed to resolve this. We can also infer that the effective f -level given by $\epsilon_f^* = Z(\epsilon_f + \Sigma(0))$ in YbIr_2Si_2 is located at roughly 25-30 meV. The dc resistivity calculated from theory for the parameters mentioned in the figure 12 does agree qualitatively with experiment in terms of a broad peak and the lineshape(see figure 9), however, the scale inferred from fitting to the experimental data does not agree with that obtained from optical conductivity. There appears to be an inconsistency in theory, in terms of an ambiguity in the parameters that

can fit the experiment. The implication is, we believe, minor. It should be possible by a better scanning of the parameter space to find a ‘right’ set of parameters that can fit the optical and dc conductivity consistently with the same scale. We believe that finding this right set of parameters will surely make the theory more convincing, but probably not by a great measure, since almost all aspects of the experiment are quantitatively captured by the presently used set of parameters. The new set of parameters would probably change the numbers (e.g for the U, V^2 values), nevertheless, the major conclusions such as that of YbIr_2Si_2 being a Fermi liquid and a mixed-valent system should remain unscathed.

6. Conclusions

We have carried out an extensive study of the changes in spectral and transport properties of the periodic Anderson model as the f -occupation number is varied from unity to nearly zero. The local moment approach within dynamical mean field theory has been employed for this study. We have used the results of our study to understand the crossover from mixed-valent regime to the Kondo lattice regime (or vice-versa) observed to occur in many rare earth intermetallics. We find several unusual features such as a two peak resistivity, anomalous absorption feature in optical conductivity etc in the crossover regime. We show that the proximity of the Hubbard band to the Fermi level is responsible for the former while the latter happens due to optical transitions into the effective f -level. The two-band (hybridization-gap) model generally applied to understand the physics of these materials is shown to be inadequate in this regime. Qualitative agreement with pressure-dependent dc resistivity measurements in CeCu_2Si_2 is found while quantitative agreement with dc transport measurements in CeRhIn_5 , $\text{Ce}_2\text{Ni}_3\text{Si}_5$, CeFeGe_3 and YbIr_2Si_2 is obtained. We also obtain excellent agreement with pressure dependent resistivity measurements in YbInAu_2 and the prototypical quantum critical system CeCu_6 . In agreement with previous observations, we find that increasing pressure pushes Cerium materials to mixed-valence while the Yb materials cross over to the Kondo lattice regime. Further, a remarkable agreement with optical conductivity experiments in YbIr_2Si_2 is obtained. We also infer from the agreement that YbIr_2Si_2 belongs to the mixed-valent regime. Further investigations including $d - f$ correlations in the periodic Anderson model are underway to understand valence transitions.

Acknowledgments

We thank Prof. David E. Logan and Prof. H. R. Krishnamurthy for discussion and useful suggestions. PK is grateful to CSIR, India for financial support.

Appendix

The expression for dynamical conductivity (hypercubic lattice) in [37] is

$$\sigma(\omega; T) = \frac{\sigma_0}{\omega} \int_{-\infty}^{\infty} d\omega_1 [n_F(\omega_1) - n_F(\omega_1 + \omega)] \int_{-\infty}^{\infty} d\epsilon \rho_0(\epsilon) D^c(\epsilon; \omega_1) D^c(\epsilon; \omega + \omega_1) \quad (12)$$

where $D^c(\epsilon; \omega) = -\text{Im}G^c(\epsilon; \omega)/\pi$; $G^c(\epsilon; \omega) = (\gamma(\omega) - \epsilon)^{-1}$ and $\gamma(\omega)$ is defined below equation 4. The identity $\text{Im}z_1\text{Im}z_2 = \text{Re}(z_1^*z_2 - z_1z_2^*)/2$ for $z_1, z_2 \in \mathbb{C}$ may be used to get

$$D^c(\epsilon; \omega_1)D^c(\epsilon; \omega + \omega_1) = \frac{1}{2\pi^2} \text{Re} \left(\frac{G^{c*}(\epsilon; \omega + \omega_1) - G^c(\epsilon; \omega_1)}{\gamma(\omega_1) - \gamma^*(\omega + \omega_1)} - \frac{G^c(\epsilon; \omega + \omega_1) - G^c(\epsilon; \omega_1)}{\gamma(\omega_1) - \gamma(\omega + \omega_1)} \right)$$

The Hilbert transform integral over ϵ in equation 12 may be carried out to give the expression 5. The $\omega \rightarrow 0$ limit of the equation 5 yields the dc conductivity. The second term involves using the L'Hopital's rule which in turn requires the knowledge of $dG^c(\omega)/d\gamma$, which we derive below. The c-Green's function is given by a Hilbert transform over the Gaussian dos. The result is expressed in terms of the complementary error function as [26]

$$G^c(\omega) = H[\gamma] = -is\sqrt{\pi} \exp(-\gamma^2) \text{erfc}(-is\gamma) \quad (13)$$

where $s = \text{sgn}(\text{Im}\gamma) = +1$ for the retarded functions considered here. The derivative of this with respect to γ is straightforward and is given by

$$\frac{dG^c(\omega)}{d\gamma} = -2\gamma G^c(\omega) - is\sqrt{\pi} \exp(-\gamma^2) (-is) \frac{d\text{erfc}(x)}{dx} \Big|_{x=-is\gamma} = 2(1 - \gamma G^c(\omega)) \quad (14)$$

Using this yields equation 6.

References

- [1] Grewe N. and Steglich F.1991 Handbook on the Physics and Chemistry of Rare Earths vol 14 ed K A Gschneider Jr. and L L Eyring (Amsterdam: Elsevier) p 343
- [2] Wachter P. 1994 Handbook on the Physics and Chemistry of Rare Earths vol 19 ed K A Gschneider and L L Eyring (Amsterdam: Elsevier) p 177
- [3] Varma C. M. 1976 Rev. Mod. Phys. **48** 219
- [4] Aeppli G. and Fisk Z. 1992 Comm. Condens. Matter Phys. **16** 155
- [5] Hewson A. C. 1993 The Kondo Problem to Heavy Fermions (Cambridge: Cambridge University Press)
- [6] Fisk Z. *et. al* 1996 Physica B **223-224** 409
- [7] Degiorgi L. 1999 Rev. Mod. Phys. **71** 687
- [8] Jaccard D., Vargoz E., Alami-Yadri K. and Wilhelm H. 1998 Rev. High Pressure Sci. Technol **7** 412
- [9] Ocko M., Geibel C. and Steglich F. 2001 Phys. Rev. B **64** 195107
- [10] Bauer E. *et. al* 1993 Phys. Rev. B **48** 15873
- [11] Kagayama T. *et. al* 1997 Physica B 230
- [12] Iizuka T. *et. al* 2010 J. Phys. Soc. Japan **79** 123703
- [13] Yuan H. Q. , Niklas M., Hossain Z., Geibel C. and Steglich F. 2006 Phys. Rev. B **74** 212403
- [14] Knebel G., Braithwaite D., Lapertot G., Canfield P. C. and Flouquet J. 2001 J. Phys. Condens. Matter **13** 10935

- [15] Matsunami M., Okamura H., Ochiai A. and Nanba T. 2009 Phys. Rev. Lett. **103** 237202
- [16] Kaczorowski D. and Slebarski A. 2010 Phys. Rev. B **81** 214411
- [17] Adroja D. T. and Rainford B. D. 1992 J. Mag. Mag. Materials. **119** 54
- [18] Kaczorowski D. *et. al* 2010 J. Phys. Condens. Matter **22** 215601
- [19] Sereni J. G. 1980 J. Phys. F: Metal Phys. **10** 2831
- [20] Franz W., Griebel A., Steglich F. and Wohlleben D. 1978 Z. Physik B **31** 7
- [21] Franz W., Steglich F. and Wohlleben D. 1979 Journal De Physique c5-342
- [22] Chandran. L, Krishnamurthy H. R. and Ramakrishnan T. V. 1992 J. Phys. Condens. Matter **4** 7067
- [23] Grewe N., Pruschke T. and Keiter H. 1988 Z. Phys. B: Condens. Matt. **71** 75
- [24] Cox D. L. and Grewe N. 1988 Z. Phys. B: Condens. Matt. **71** 321
- [25] Coleman P. 1984 Phys. Rev. B **29** 3035
- [26] Georges A., Kotliar G., Krauth W. and Rozenberg M. 1996 Rev. Mod. Phys. **68** 13
- [27] Pruschke T., Jarrell M. and Freericks J. 1995 Adv. Phys. **44** 187
- [28] Llewellyn Smith J. and Qimiao Si 1997 arXiv:cond-mat/9705140v1 [cond-mat.str-el]
- [29] Maier T., Jarrell M., Pruschke T., and Hettler M. H. 2005 Rev. Mod. Phys. **77** 1027
- [30] Scalettar R. T., Scalapino D. J. and Sugar R. L. 1985 Phys. Rev. B 7316
- [31] Pruschke T., Bulla R. and Jarrell M., Phys. Rev. B 2000 **61** 12799
- [32] Jarrell M. 1995 Phys. Rev. B **51** 7429
- [33] Rozenberg M. J. 1995 Phys. Rev. B **52** 7369 R3332 (1997)
- [34] Vidhyadhiraja N. S. , Tahvildar-Zadeh A. N. , Jarrell M. and Krishnamurthy H. R. 2000 Europhys. Lett. **49** 459
- [35] Vidhyadhiraja N. S. and Logan D. E. 2004 Eur. Phys. J. B **39** 313-334
- [36] S. J. Sun, M.F. Yang and T. M. Hong, Phys. Rev. B **48** (1993) 16127
- [37] Logan D. E. and Vidhyadhiraja N. S. 2005 J. Phys. Condens. Matter **17** 2935
- [38] Vidhyadhiraja N. S. and Logan D. E. 2005 J. Phys. Condens. Matter **17** 2959
- [39] Glossop M. T. and Logan D. E. 2002 J. Phys. Condens. Matter **14** 6737
- [40] Sun P. and Kotliar G. 2005 Phys. Rev. Lett. **95** 016402
- [41] Logan D. E. , Eastwood M. P. and Tusch M. A. 1998 J. Phys. Condens. Matter **10** 2673
- [42] Bulla R. , Glossop M. T. , Logan D. E. and Pruschke T. 2000 J. Phys. Condens. Matter **12** 4899
- [43] Vidhyadhiraja N. S. , Smith V. E. , Logan D. E. and Krishnamurthy H. R. 2003 J. Phys. Condens. Matter **15** 4045-4087
- [44] Gilbert A., Vidhyadhiraja N. S. and Logan D. E. 2007 J. Phys. Condens. Matter **19** 106220
- [45] Freericks J. K. and Zlatic V. 2001 Phys. Rev. B **64** 245118
- [46] Bernhard B. H. and Coqblin B. 2009 Physica B **404** 3021
- [47] Watanabe S., Imada M., Miyake K. 2006 J. Phys. Soc. Japan **75** 043710
- [48] Sugibayashi T. and Hirashima D. S. 2006 J. Phys. Soc. Japan **75** 244-246
- [49] Ylvisaker E. R. , Kunes J. , McMahan A. K. and Pickett W. E. 2009 Phys. Rev. Lett. **102** 246401
- [50] Economou E. N. 1983 Green's Functions in Quantum Mechanics (Berlin: Springer)
- [51] Okamura H. *et. al* 2007 J. Phys. Soc. Japan **76** 023703.
- [52] Bucher. B *et. al* 1996 Phys. Rev. B **53** R2948.
- [53] Kimura Shin-ichi 2009 Phys. Rev. B **80** 073103
- [54] Kajueter. H and Kotliar. G, 1996 Phys. Rev. Lett. **77** 131.
- [55] Christianson A. D. *et. al* 2002 Phys. Rev. B **66** 054410
- [56] Chandan Mazumdar *et. al* 1992 Phys. Rev. B **46** 9009
- [57] Bud'ko S. L. *et. al* 1998 J. Phys. Condens. Matter **10** 8815
- [58] Fuse A. *et. al* 2000 Physica B **281&282** 175
- [59] Thompson J. D. and Fisk Z. 1985 Phys. Rev. B **31** 389
- [60] Hossain Z. *et. al* 2005 Phys. Rev. B **72** 094411